Short communication

A novel approach to obtain highly intense self-activated photoluminescence emissions in hydroxyapatite nanoparticles

Thales R. Machado[a,b], Júlio C. Sczancoski[a], Héctor Beltrán-Mir[b], Içamira C. Nogueira[c], Máximo S. Li[d], Juan Andrés[e], Eloisa Cordoncillo[b], Elson Longo[a,*]

[a] CDMF-UFSCar, Universidade Federal de São Carlos, P.O. Box 676, 13565-905 São Carlos, São Paulo, Brazil
[b] QIO-UJI, Universitat Jaume I, 12071 Castellón, Spain
[c] PPGEM-IFMA, Instituto Federal de Educação, Ciência e Tecnologia do Maranhão, 65030-005 São Luís, MA, Brazil
[d] IFSC-USP, Universidade de São Paulo, P.O. Box 369, 13560-970 São Carlos, SP, Brazil
[e] QFA-UJI, Universitat Jaume I, 12071 Castellón, Spain

ARTICLE INFO

ABSTRACT

Defect-related photoluminescence (PL) in materials have attracted interest for applications including near ultraviolet (NUV) excitable light-emitting diodes and in biomedical field. In this paper, hydroxyapatite [$Ca_{10}(PO_4)_6(OH)_2$] nanorods with intense PL bands (bluish- and yellowish-white emissions) were obtained when excited under *NUV radiation* at room temperature. These nanoparticles were synthesized via chemical precipitation at 90 °C followed by distinct heat treatments temperatures (200–800 °C). Intense and broad emission profiles were achieved at 350 °C (380–750 nm) and 400 °C (380–800 nm). UV–Vis spectroscopy revealed band gap energies (5.58–5.78 eV) higher than the excitation energies (~3.54 and ~2.98 eV at 350 and 415 nm, respectively), confirming the contribution of defect energy levels within the forbidden zone for PL emissions. The structural features were characterized by X-ray diffraction, Rietveld refinement, thermogravimetric analysis, and Fourier transform infrared spectroscopy. By means of these techniques, the relation between structural order-disorder induced by defects, chemical reactions at both lattice and surface of the materials as well as the PL, without activator centers, was discussed in details.

1. Introduction

Scientific research focused on luminescent materials has strategic importance for the development of the next generation of optical devices, including sensors, thermometers, photodetectors, light-emitting diodes (LEDs) [1–4]. White LEDs (WLEDs) are promising devices for the replacement of traditional incandescent or fluorescent lamps because of their power savings, longer lifetime, higher luminous efficiency, brightness, and environmental friendliness [5]. The typical approach to obtain WLEDs is based on the use of single- or multi-phase phosphors coupled with a near-ultraviolet (NUV, 350–415 nm) radiation source [6]. These types of phosphors are commonly doped with single or multiple activator ions (Eu^{2+}, Ce^{3+}, Yb^{3+}, and Tb^{3+}) to enhance their optical activities. However, minimizing the use of these elements is of interest because of the high cost involved in their production.

As an alternative, non-toxic materials with intense defect-related photoluminescence (PL) have been investigated for the manufacture of new optical devices [7–11]. Among these materials, a good luminescent material candidate for this purpose is hydroxyapatite [HA, $Ca_{10}(PO_4)_6(OH)_2$]. HA is a well-known calcium orthophosphate with unique in vivo behavior, including biocompatibility and bioactivity [12]. For biomedical applications, the luminescence of HA can be improved with the insertion of low concentrations of lanthanides (Eu^{2+}, Eu^{3+}, and Tb^{3+} ions) in the host material, especially because of the $4f \rightarrow 4f$ and $4f5d \rightarrow 4f$ transitions [13–17]. However, in terms of crystalline structure, HA is significantly flexible, i.e., the lattice can stabilize large amounts of ionic substitutions in each of its sites as well as vacancies, structural defects, and distortions. This feature can be explored to obtain efficient, stable, and broad band self-activated blue emissions (λ_{max}=420 nm) [18]. In recent studies [19–21], this blue PL of HA nanoparticles, without the presence of activators, has been successfully used for biomedical applications. In addition, Ce^{3+} and Mn^{2+}-codoped HA has been demonstrated to be a suitable phosphor to fabricate stable WLEDs because of the ultraviolet and yellow luminescence emissions departing from the activators combined with the intrinsic blue emission of HA nanoparticles [22].

Today, the development of a facile synthesis method for the

formation of HA nanoparticles with intense self-activated emissions located in the visible spectrum region, without the necessity of using other activator ions in the matrix, has become an increasing challenge for scientists. Moreover, as HA exhibits a complex defective structure, the main energy states responsible for radiative emissions are unclear. The precise control and manipulation of these energy levels could allow tunable colors to be obtained, which are of great interest for the technological industries. Specially, HA is affected by several mechanisms associated with heating, such as the gradual elimination and decomposition of entrapped species, introduction of new species arising from the atmosphere, increase of the degree of structural ordering in the lattice, and sintering processes [23]. These phenomena can modify its electronic structure and charge distribution. Therefore, the aim of the present study was to experimentally investigate the effect of heat treatments on the structural features and self-activated PL of chemically precipitated HA. Moreover, it was described the preparation of HA nanoparticles with intense bluish- and yellowish-white PL emissions when excited under NUV radiation.

2. Experimental section

2.1. Synthesis of HA nanoparticles

The HA samples were prepared via chemical precipitation in a basic environment. Calcium nitrate tetrahydrate $[Ca(NO_3)_2 \cdot 4H_2O]$ (99%, Sigma Aldrich) and di-ammonium phosphate $[(NH_4)_2HPO_4]$ (98+%, Strem Chemicals) were used as precursors. Ammonium hydroxide $[NH_4OH]$ was employed to control the pH, and *Milli-Q* water was used as a solvent. First, 50 mL of an aqueous solution containing 10 mmol of Ca^{2+} ions, and 100 mL of an aqueous solution containing 6 mmol of the phosphate precursor were prepared. Then, the pH of both solutions was adjusted to 9.5–10.0 by adding NH_4OH. The prepared solutions were mixed by the dropwise addition of the phosphate precursor to the Ca^{2+} solution at an approximate rate of 7 mL/min using a peristaltic pump. The mixture was then ripened for 2 h. The temperature was maintained at 90 °C during both the synthesis and ripening step. The milky suspension obtained was washed several times with *Milli-Q* water and ethanol and centrifuged (8000 rpm). The resulting powder was dried at 80 °C for 24 h under air atmosphere. The sample obtained is referred to as the raw sample.

2.2. Heat treatments of HA nanoparticles

The obtained raw sample was heat treated in a furnace under air atmosphere at 200 °C, 300 °C, 350 °C, 400 °C, 450 °C, 500 °C, 600 °C and 800 °C for 4 h. The heating rate was maintained at 5 °C/min for all the temperature conditions. The samples were naturally cooled to room temperature. The experimental procedure is schematically presented in Scheme 1.

2.3. Characterization

The raw sample and those heat treated at different temperatures were structurally characterized by X-ray diffraction (XRD) in a

Shimadzu XRD-6000 (Japan) diffractometer using *Cu Kα* radiation (λ=0.154184 nm). Data were collected over 2θ values ranging from 20° to 70° using a step scan rate and step size of 0.2°/min and 0.02°, respectively. For the Rietveld refinements, data were collected over 2θ values ranging from 5° to 110°. For detailed description of the refinements, see the Supplementary material.

Fourier transform infrared (FTIR) spectroscopy was performed at room temperature using a Jasco FT/IR-6200 (Japan) spectrophotometer operated in absorbance mode. Spectra were recorded at a resolution of $4 \, cm^{-1}$ over wavenumbers ranging from 400 to $4000 \, cm^{-1}$. These measurements were performed on 12-mm-diameter pellets, which were composed of 1 wt% of each sample mixed with 99 wt% of KBr (≥99%, Sigma Aldrich).

Thermogravimetric (TG) analysis was performed using a Netzsch TG 209 F1 Iris (Germany) thermo-microbalance. The temperature range used was from 25 °C to 800 °C at a heating rate of 10 °C/min under synthetic air atmosphere (5 mL/min of O_2 and 15 mL/min of N_2) using an alumina crucible.

UV–vis spectroscopy was performed using a Varian Cary 5 G (USA) spectrophotometer operated in diffuse-reflection mode. The standard samples in the reflectance measurements were SRS-80-010 and SRS02-010 for white and black standards from *Labsphere* [24], respectively. Detailed description for the methodology used to estimate the band gap energies is available in the Supplementary material.

The morphological features were examined by field-emission scanning electron microscopy (FE-SEM) with a Carl Zeiss Supra 35-VP (Germany) microscope operated at 5 kV. The nanoparticle dimensions were estimated using distinct FE-SEM images collected from the sample heat treated at 400 °C; the number of counting require for statistical analyses were 100 nanoparticles. Transmission electron microscopy (TEM) and high-resolution transmission electron microscopy (HRTEM) micrographs as well as selected area electron diffraction (SAED) and energy-dispersive X-ray spectroscopy (EDS) analysis were performed with a FEI TECNAI F20 (Netherlands) microscope operating at 200 kV.

PL spectroscopy was conducted at room temperature using a Thermal Jarrel Ash Monospec 27 (USA) monochromator coupled to a Hamamatsu R955 (Japan) photomultiplier. A Coherent Innova 200 K krypton ion laser (USA) (λ_{exc}=350 and 415 nm) was used as an excitation source. The incident laser beam on each sample was maintained at a maximum power of 15 and 7 mW at λ_{exc}=350 nm and 415 nm, respectively.

3. Results and discussion

3.1. Structural and morphological characterization

The identification of the crystalline phases of all the samples with the evolution of the heat treatment temperature was performed using XRD, and the results are presented in Fig. 1(a). The diffraction peaks are related to the hexagonal HA phase (space group $P6_3/m$), which is consistent with the results reported in the Inorganic Crystal Structure Data (ICSD) base No. 26204 [25]. No secondary phases were observed in these samples, even after heat treatment. The narrow profiles of the

Precipitated HA nanorods   →(Heat Treatment)→   **HA nanorods with enhanced PL**
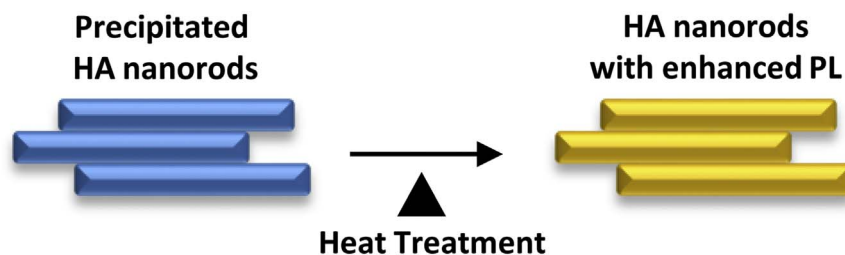
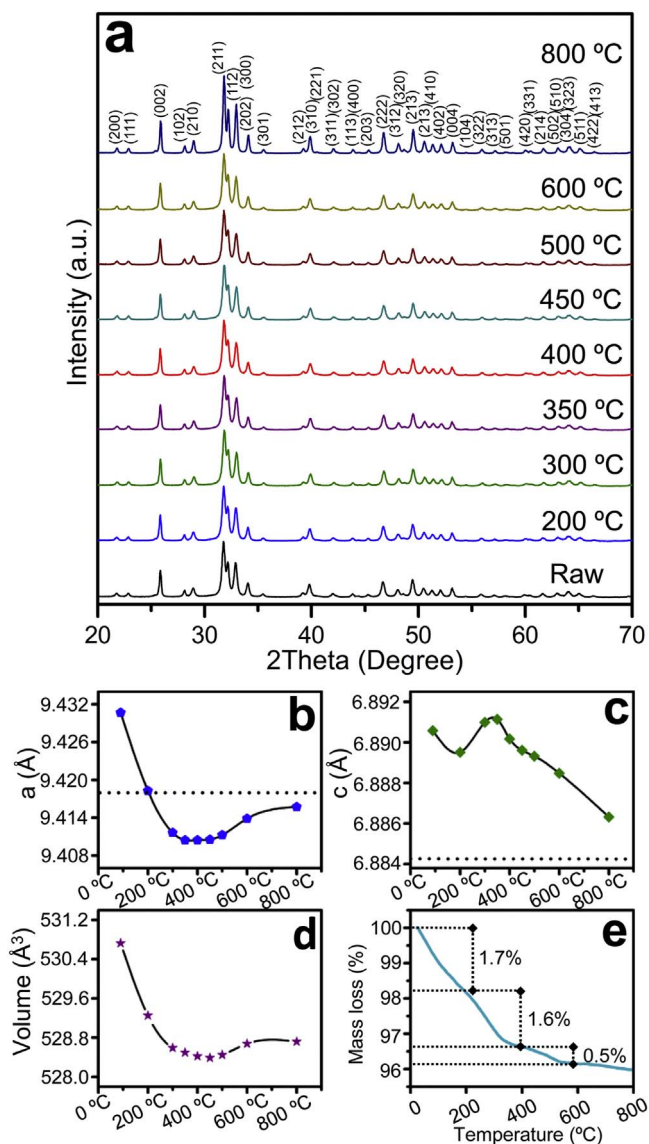**Scheme 1.** Preparation of HA nanorods with improved PL emissions.

Fig. 1. Structural characterization of HA samples: (a) XRD patterns, (b) a lattice parameter, (c) c lattice parameter, (d) unit cell volume, and (e) TG curve. The dashed line refers to the unit cell parameters of pure HA from Ref. [26].

Fig. 2. FTIR spectra (a) of all the samples, (b) the region from 3000 to 3650 cm^{-1}, and (c) the region from 750 to 950 cm^{-1}.

diffraction peaks at 800 °C are related to an increase of long-range structural ordering.

The structural behavior of the HA samples was also analyzed by Rietveld refinement. The plots in Fig. S1(a–i) are in perfect agreement with the XRD patterns presented in Fig. 1(a). In Table S1, the fitting parameters (R_{wp}, R_p, R_{Bragg}, χ^2) revealed a good adjust between the theoretical and observed XRD patterns. Fig. 1(b–d) presents the calculated values for the unit cell parameters obtained using the refinements. Significant variations in the lattice parameters and unit cell volume were detected, i.e., expansions and contractions of the crystalline lattice. First, the *a* and *c* parameters for the raw sample were higher than those found in the literature (*a*=9.418 Å and *c*=6.884 Å [26]). The reason for this difference is directly related to the existence of minority species trapped in HA lattice, which have higher ionic radii than Ca, PO$_4$, or OH. Further discussion is mainly focused on the *a* parameter, which is more subtly affected by the presence of impurities and structural changes induced by the heating than *c* parameter. A common impurity observed in precipitated HA is structural CO$_3^{2-}$. However, the presence of this group results in contraction of the *a* parameter [27]. Actually, the unit cell expansion is accompanied by the
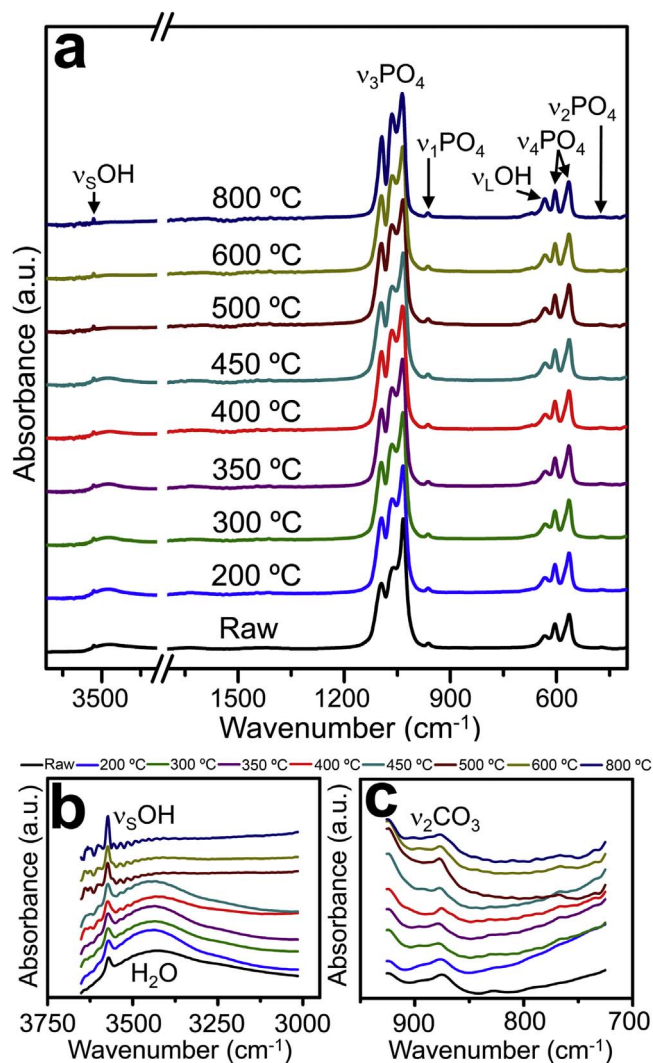
presence of water molecules in the lattice, and NH$_4^+$ groups substituting Ca atoms (the ionic radii of NH$_4^+$ and Ca are 1.43 and 0.99 Å, respectively) [28,29]. The subsequent and abrupt decrease of the *a* parameter in HA samples heat treated up to 350 °C is caused by the so-called liberation of "entrapped" water molecules [30]. Moreover, NH$_4^+$ species can also decompose in this range of temperature according to the reaction HA + NH$_4^+$ → HA...H$^+$+ NH$_3$↑ [29]. In these cases, vacancies and HA...H$^+$ species will remain in the HA structure, promoting a contraction in the unit cell. From 450 to 800 °C, there is a convergence of the unit cell parameters to values close to those of pure HA. This phenomenon is caused by the increase in the degree of long-range structural ordering in the HA lattice. The thermal decomposition behavior of our samples was also characterized by thermogravimetric analysis (TG), as shown in Fig. 1(e). The TG profile indicates a total mass loss of 3.8 wt%, which can be divided into three main weight loss regions. The first two regions (1.7 and 1.6 wt%), located from 0 to 400 °C, are caused by the liberation of physisorbed and/or entrapped water and NH$_3$. The last region (0.5 wt%), observed from 400 to 600 °C, is arising from the decomposition of other impurities in the structure, such as carbonates [30].

The HA samples were also analyzed using FTIR spectroscopy. Fig. 2 presents the FTIR spectra of (a) all the HA samples, (b) the region from 3000 to 3650 cm^{-1}, and (c) the region from 750 to 950 cm^{-1}. All the vibrational bands in our samples are frequently observed in HA

samples, including the [PO$_4$] bands at 471 cm^{-1} (v$_2$), 563 and 604 cm^{-1} (v$_4$), 963 cm^{-1} (v$_1$), 1033 cm^{-1}, 1063 cm^{-1}, and 1096 cm^{-1} (v$_3$) and the bands at 633 and 3568 cm^{-1} arising from the librational (v$_L$) and stretching (v$_S$) modes of OH groups, respectively [31]. In the raw sample, weak bands related to structural CO$_3^{2-}$ were also observed at 880 cm^{-1} (v$_2$, A-type substitution, OH$^-$→CO$_3^{2-}$), 875 cm^{-1} (v$_2$, B-type substitution, PO$_4^{3-}$→CO$_3^{2-}$), and 1418–1540 cm^{-1} (v$_3$, A+B) [32]. This result indicates that the product of the precipitation is a slightly AB-type carbonated HA. However, the bands of CO$_3^{2-}$ in A-sites were not observed at 400 °C, confirming its elimination from the lattice (for example, by the reaction CO$_3^{2-}$+H$_2$O→2OH$^-$+CO$_2$), whereas those in B-sites remained in all the samples [28]. Other important changes in the samples were observed with the heat treatment. The OH bands showed a slight increase in intensity (especially after 450 °C), which is associated with the incorporation of OH groups in the structure (Fig. 2b). It is well-known that the initially precipitated HA contains a significant density of OH vacancies related to crystal disorder and/or the presence of CO$_3^{2-}$ [29]. However, these vacancies disappear once heat treated because of the decomposition of carbonate or the hydroxylation process originating from the hydrolysis of adsorbed water molecules at the HA surface. In addition, the v$_3$PO$_4$ modes become gradually more defined and intense, reflecting the increase in the short-range ordering in the lattice (Fig. 2a).

Fig. 3(a) presents a FE-SEM image of the HA sample heat treated at 400 °C and the estimation of the nanoparticle dimensions. For the FE-SEM images of the other samples, see Fig. S2(a–h) in the Supplementary material. Typical HA nanorods with 300–600 nm in
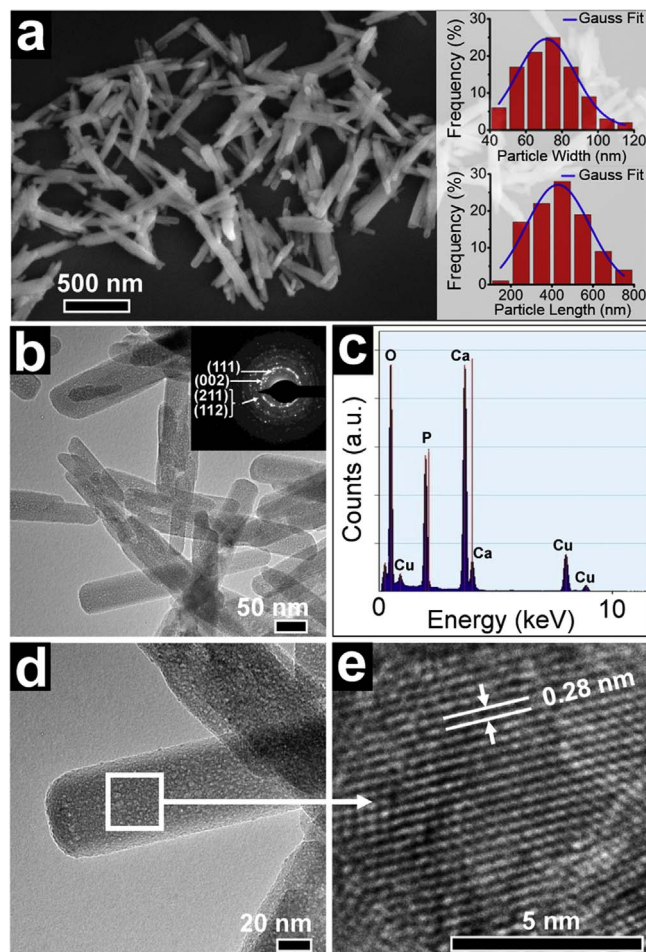
Table 1
Optical *Eg* and CIE chromaticity coordinates of HA samples.

Sample	Optical E_g (eV)	x coordinate (λ_{exc}=350 nm/415 nm)	y coordinate (λ_{exc}=350 nm/415 nm)
Raw	5.58	0.18/0.21	0.26/0.44
200 °C	5.56	0.21/0.23	0.33/0.48
300 °C	5.63	0.25/0.26	0.36/0.48
350 °C	5.60	0.35/0.32	0.38/0.47
400 °C	5.64	0.45/0.44	0.40/0.44
450 °C	5.61	0.50/0.50	0.38/0.41
500 °C	5.58	0.41/0.45	0.35/0.43
600 °C	5.59	0.22/0.24	0.28/0.44
800 °C	5.78	0.23/0.21	0.34/0.47

length and 40–80 nm in width were observed. However, from 600 to 800 °C, an initial stage of sintering was verified in this system (matter transport and densification between the nanorods). A TEM image for the HA sample heat treated at 400 °C is presented in Fig. 3(b). The selected area electron diffraction (SAED) pattern of this micrograph (inset in Fig. 3(b)) reveals the occurrence of concentric rings, which were indexed to (111), (002), (211), and (112) planes of the hexagonal HA phase. This type of SAED pattern is typically observed in materials with a polycrystalline nature. EDX analysis in Fig. 3(c) confirms that the main elements present are Ca and P. Fig. 3(d,e) presents a high-magnification TEM image and high-resolution TEM (HRTEM) analysis performed on a single nanorod, respectively. In these figures, the interplanar distance of 0.28 nm corresponds to the (211) plane of HA.

3.2. Electronic structure and optical properties

The band gap energy (E_g) of all the HA samples obtained by UV–vis spectroscopy are listed in Table 1. The methodology employed for this estimation as well as the calculated plots are presented in the Supplementary material (Fig. S3(a–i)). High E_g values from 5.58 to 5.78 eV were observed in these samples. An increase of E_g with the evolution of the heat treatment temperature is observed, which implies that the temperature plays a crucial role in the relaxation of defects (surface and bulk) as well as in the increase of structural ordering of HA lattice.

In this study, our HA samples were sensitive to different excitation wavelengths in the NUV region. PL spectra of the HA samples were first measured under excitation at 350 nm (Fig. 4(a)). The *Commission internationale de l'éclairage* (CIE) chromaticity coordinates are listed in Table 1. The PL spectrum of the raw sample exhibited a maximum intensity at approximately 440 nm, resulting in a blue emission (digital image in Fig. 4(c)). This PL profile is similar to those observed for other HAs [18,33,34]. When the samples were heat treated at 200 and 300 °C, a slight shift of the maximum emission to 470 nm as well as an increase in the PL intensity were observed. The highest PL emissions were evidenced in HA samples heat treated at 350 and 400 °C. An important feature in these spectra is the broad band profile, which covers a large part of the visible electromagnetic spectrum (380–750 nm at 350 °C, and 380–800 nm at 400 °C). In these respective heat treatment temperatures, the maximum PL centers were found at 530 and 580 nm; therefore, there is a predominance of intense bluish- and yellowish-white emissions (Fig. 4(c)). However, after the heat treatments performed at 450 °C, 500 °C, 600 °C, and 800 °C, a suppression of the PL emission occurred (Fig. 4(a,c)). This experimental observation supports the concept on the dependence of the structural ordering and PL response on the temperature.

Fig. 4(b) presents the PL spectra of all the HA samples measured with less energetic NUV wavelengths (415 nm). The CIE chromaticity coordinates are listed in Table 1. When excited at 415 nm, the PL behavior of the HA samples is very similar to that observed under excitation of 350 nm. However, there is a slight shift in the relative

Fig. 3. Morphological characterization of HA sample heat treated at 400 °C: (a) FE-SEM image and the estimation of nanoparticle dimensions (inset), (b) TEM image and the respective SAED analysis (inset), (c) EDX analysis, (d) high-magnification TEM image of a single nanorod, and (e) HRTEM image.
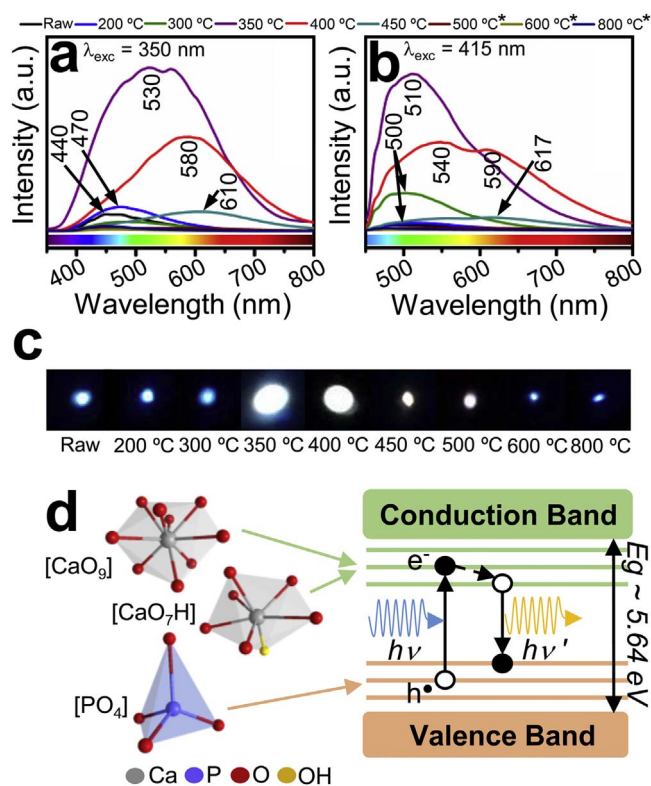
Fig. 4. Optical behavior of HA: (a) PL emission under excitation at λ_{exc}=350 nm, (b) PL emission under excitation at λ_{exc}=415 nm, (c) digital images of HA samples under excitation at λ_{exc}=350 nm, and (d) schematic of band structure for HA samples, considering the contribution of coordination clusters of the HA structure to defective energy levels within the band gap; $e'–h^{\bullet}$ recombination process via simple radiative/non-radiative decay. The low-intensity PL emission of the HA samples at 500 °C, 600 °C and 800 °C present overlapped profiles (*).

[CaO_9] clusters. In contrast, the Ca(2) site is surrounded by six O atoms of [PO_4] clusters and one OH inside the hexagonal channels of the structure, leading to [CaO_7H] clusters [25]. Based on the above results, the formation and organization of the energy levels within the band gap are directly associated with the symmetry break [35] in these clusters (changes in both P−O and Ca−O bond angles and lengths from their equilibrium positions) induced by the defects (impurities, vacancies, and/or lattice disorder) observed in HA samples (Fig. 4(e)). Hence, the behavior caused by the heat treatment performed on the precipitated HA could be related to order−disorder changes induced by the peculiarity of this structure, in which there is a high density of entrapped impurities and vacancies. Moreover, the concentration of HA...H$^+$ and OH vacancies can play crucial roles in the electronic densities of neighbor Ca and P clusters. It is well-known that the species near and inside of the hexagonal channels of HA structure significantly modify the physicochemical properties of HA [36]. Moreover, the distortions in the structure related to HA...H$^+$ and OH vacancies cause extra semi-filled levels near the valence and conduction bands, enhancing the radiative electron−hole ($e'−h^{\bullet}$) recombination processes [33,37].

In summary, among the other defects, the increase in the density of HA...H$^+$ from the raw sample to 350 °C leads to extra disorder in the lattice with the presence of OH vacancies. Therefore, a high density of shallow- and deep-level defect states is generated within the band gap of the HA samples treated at 350 and 400 °C, resulting in a broad band bluish- and yellowish-white emissions, respectively. At 400 °C, CO_3^{2-} substituting for OH groups and its decomposition could also contribute to the appearance of additional energy levels. At high heat treatment temperatures (from 450 to 800 °C), the structural order increased significantly in the HA samples because of the accommodation of species in their equilibrium positions in the lattice, elimination of impurities, and introduction of OH inside the channels. All these factors minimize the defect energy levels within the band gap, reducing or completely suppressing the PL emissions.

4. Conclusions

The effect of posterior heat treatments on the structural and optical properties of HA nanorods prepared via chemical precipitation was studied. Depending on the temperature (200 °C, 300 °C, 350 °C, 400 °C, 450 °C, 500 °C, 600 °C, and 800 °C), changes in the intensities and PL emission profiles were observed. The most intense self-activated bluish- and yellowish-white emissions under NUV excitation were achieved for the sample heat treated at 350 and 400 °C, respectively. The intrinsic PL arose from the $e'−h^{\bullet}$ recombination between defect energy levels within the band gap. This behavior was observed by using excitation energies (~3.54 and ~2.98 eV at 350 and 415 nm, respectively) lower than the E_g values (from 5.58 to 5.78 eV) observed in the samples. Structural characterization revealed the presence of defects and intrinsic impurities in the samples. By heating, chemical reactions in the lattice as well as at the surfaces occurred, significantly changing the electronic structure of HA samples.

Appendix A. Supporting information

Supplementary data associated with this article can be found in the online version at doi:10.1016/j.jssc.2016.12.018.

positions of the maximum emission centers of the samples for this excitation source. For example, for the raw sample, the maximum intensity was observed at 477 nm, whereas for those heat treated at 200 and 300 °C the maximum intensity was detected at 500 nm. Although maintaining the feature of a broad PL band at 350 °C (420–750 nm) and 400 °C (420–800 nm), the spectra of these heat treated HA samples revealed the existence of a maximum emission center at 510 nm, and two others situated at around 540 and 590 nm, respectively.

Hence, the shape and intensity of the PL emission in this study varied significantly with the heat treatment temperature and excitation wavelength. The variations in both the x and y CIE chromaticity coordinates listed in Table 1 with the heating temperature and in y when changing the NUV source confirm the tunable PL emissions of HA nanoparticles.

3.3. Possible origins for the PL emissions in heat treated HA

In this case, it is reasonable to assume that the wide band emission originates from electronic transitions involving the participation of several energy states within the forbidden zone or band gap. This explication is justified because the excitation sources employed in this study have lower energies (~3.54 and ~2.98 eV at 350 and 415 nm, respectively) than the E_g (from 5.58 to 5.78 eV) verified in the HA samples. In previous publications [33,34], possible mechanisms responsible for blue emissions in HA have been proposed. However, information on the PL behavior observed in our study is scarce.

In fact, the arrangement of [PO_4] clusters in the HA structure provides two distinct crystallographic sites for Ca species. The Ca(1) site is surrounded by nine O atoms belonging to [PO_4], resulting in

References

[1] Y. Cui, H. Xu, Y. Yue, Z. Guo, J. Yu, J. Chen, J. Gao, Y. Yang, G. Qian, B. Chen, J. Am. Chem. Soc. 134 (2012) 3979–3982.

[2] Y. Ma, S. Wang, L. Wang, Trends Anal. Chem. 65 (2015) 13–21.

[3] S. Nakamura, T. Mukai, M. Senoh, Appl. Phys. Lett. 64 (1994) 1687–1689.

[4] X. Zhou, L. Gan, Q. Zhang, X. Xiong, H. Li, Z. Zhong, J. Han, T. Zhai, J. Mater. Chem. C 4 (2016) 2111–2116.

[5] P.F. Smet, A.B. Parmentier, D. Poelman, J. Electrochem. Soc. 158 (2011) R37–R54.

[6] M. Shang, C. Li, J. Lin, Chem. Soc. Rev. 43 (2014) 1372–1386.

[7] A.M. Jakob, T.A. Schmedake, Chem. Mater. 18 (2006) 3173–3175.

[8] C.K. Lin, Y. Luo, H. You, Z. Quan, J. Zhang, J. Fang, J. Lin, Chem. Mater. 18 (2006) 458–464.

[9] S.K. Gupta, P.S. Ghosh, N. Pathak, R. Tewari, RSC Adv. 5 (2015) 56526–56533.

[10] T. Ogi, Y. Kaihatsu, F. Iskandar, W.-N. Wang, K. Okuyama, Adv. Mater. 20 (2008) 3235–3238.

[11] B. Sundarakannan, M. Kottaisamy, Mater. Lett. 165 (2016) 153–155.

[12] M. Vallet-Regí, J.M. González-Calbet, Prog. Solid State Chem. 32 (2004) 1–31.

[13] B. Ma, S. Zhang, J. Qiu, J. Li, Y. Sang, H. Xia, H. Jiang, J. Claverie, H. Liu, Nanoscale 8 (2016) 11580–11587.

[14] X. Zheng, M. Liu, J. Hui, D. Fan, H. Ma, X. Zhang, Y. Wang, Y. Wei, Phys. Chem. Chem. Phys. 17 (2015) 20301–20307.

[15] M. Liu, H. Liu, S. Sun, X. Li, Y. Zhou, Z. Hou, J. Lin, Langmuir 30 (2014) 1176–1182.

[16] Z. Hou, P. Yang, H. Lian, L. Wang, C. Zhang, C. Li, R. Chai, Z. Cheng, J. Lin, Chem. Eur. J. 15 (2009) 6973–6982.

[17] P. Yang, Z. Quan, C. Li, X. Kang, H. Lian, J. Lin, Biomaterials 29 (2008) 4341–4347.

[18] G.S. Kumar, E.K. Girija, Ceram. Int. 39 (2013) 8293–8299.

[19] C. Wang, D. Liu, C. Zhang, J. Sun, W. Feng, X.-J. Liang, S. Wang, J. Zhang, ACS Appl. Mater. Interfaces 8 (2016) 11262–11271.

[20] R.K. Singh, T.-H. Kim, K.D. Patel, J.-J. Kim, H.-W. Kim, J. Mater. Chem. B 2 (2014) 2039–2050.

[21] C. Zhang, C. Li, S. Huang, Z. Hou, Z. Cheng, P. Yang, C. Peng, J. Lin, Biomaterials 31 (2010) 3374–3383.

[22] C. Zhang, S. Huang, D. Yang, X. Kang, M. Shang, C. Peng, J. Lin, J. Mater. Chem. 20 (2010) 6674–6680.

[23] S. Raynaud, E. Champion, D. Bernache-Assollant, P. Thomas, Biomaterials 23 (2002) 1065–1072.

[24] Labsphere webpage. ⟨http://www.labsphere.com⟩ (accessed 09.07.16).

[25] K. Sudarsanan, R.A. Young, Acta Crystallogr. B25 (1969) 1534–1543.

[26] T.S.B. Narasaraju, D.E. Phebe, J. Mater. Sci. 31 (1996) 1–21.

[27] I.R. Gibson, W. Bonfield, J. Biomed. Mater. Res. 59 (2002) 697–708.

[28] Z.Z. Zyman, D.V. Rokhmistrov, V.I. Glushko, I.G. Ivanov, J. Mater. Sci. Mater. Med. 20 (2009) 1389–1399.

[29] J.C. Elliot, Studies in inorganic chemistry. Vol 18. Structure and Chemistry of the Apatites and Other Calcium Orthophosphates, Elsevier, Amsterdam, 1994.

[30] K. Tõnsuaadu, K.A. Gross, L. Plūduma, M. Veiderma, J. Therm. Anal. Calorim. 110 (2012) 647–659.

[31] B.O. Fowler, Inorg. Chem. 13 (1974) 194–207.

[32] S. Marković, L. Veselinović, M.J. Lukić, L. Karanović, I. Bračko, N. Ignjatović, D. Uskoković, Biomed. Mater. 6 (2011) 045005.

[33] A.V. Bystrova, Y.D. Dekhtyar, A.I. Popov, J. Coutinho, V.S. Bystrov, Ferroelectrics 475 (2015) 135–147.

[34] C. Zhang, J. Yang, Z. Quan, P. Yang, C. Li, Z. Hou, J. Lin, Cryst. Growth Des. 9 (2009) 2725–2733.

[35] M. Anicete-Santos, E. Orhan, M.A.M.A. de Maurera, L.G.P. Simões, A.G. Souza, P.S. Pizani, E.R. Leite, J.A. Varela, A. Beltrán, E. Longo, Phys. Rev. B 75 (2007) 165105.

[36] V. Uskoković, RSC Adv. 5 (2015) 36614–36633.

[37] K. Matsunaga, A. Kuwabara, Phys. Rev. B 75 (2007) 014102.